Structural Influence of Hydrophobic Core Residues on Metal Binding and Specificity in Carbonic Anhydrase II[†,‡]

J. David Cox,[§] Jennifer A. Hunt,[||] Kevin M. Compher,[§] Carol A. Fierke,*[,||] and David W. Christianson*[,§]

Roy and Diana Vagelos Laboratories, Department of Chemistry, University of Pennsylvania, Philadelphia, Pennsylvania 19104-6323, and Department of Chemistry, University of Michigan, Ann Arbor, Michigan 48109-1055

Received July 14, 2000; Revised Manuscript Received September 8, 2000

ABSTRACT: Aromatic residues in the hydrophobic core of human carbonic anhydrase II (CAII) influence metal ion binding in the active site. Residues F93, F95, and W97 are contained in a β-strand that also contains two zinc ligands, H94 and H96. The aromatic amino acids contribute to the high zinc affinity and slow zinc dissociation rate constant of CAII [Hunt, J. A., and Fierke, C. A. (1997) *J. Biol. Chem.* 272, 20364−20372]. Substitution of these aromatic amino acids with smaller side chains enhances Cu^{2+} affinity while decreasing Co^{2+} and Zn^{2+} affinity [Hunt, J. A., Mahiuddin, A., & Fierke, C. A. (1999) *Biochemistry* 38, 9054−9062]. Here, X-ray crystal structures of zinc-bound F93I/F95M/W97V and F93S/F95L/W97M CAIIs reveal the introduction of new cavities in the hydrophobic core, compensatory movements of surrounding side chains, and the incorporation of buried water molecules; nevertheless, the enzyme maintains tetrahedral zinc coordination geometry. However, a conformational change of direct metal ligand H94 as well as indirect (i.e., "second-shell") ligand Q92 accompanies metal release in both F93I/F95M/W97V and F93S/F95L/W97M CAIIs, thereby eliminating preorientation of the histidine ligands with tetrahedral geometry in the apoenzyme. Only one cobalt-bound variant, F93I/F95M/W97V CAII, maintains tetrahedral metal coordination geometry; F93S/F95L/W97M CAII binds Co^{2+} with trigonal bipyramidal coordination geometry due to the addition of azide anion to the metal coordination polyhedron. The copper-bound variants exhibit either square pyramidal or trigonal bipyramidal metal coordination geometry due to the addition of a second solvent molecule to the metal coordination polyhedron. The key finding of this work is that aromatic core residues serve as anchors that help to preorient direct and second-shell ligands to optimize zinc binding geometry and destabilize alternative geometries. These geometrical constraints are likely a main determinant of the enhanced zinc/copper specificity of CAII as compared to small molecule chelators.

Carbonic anhydrase II (CAII)[1] is a zinc metalloenzyme that catalyzes the reversible hydration of carbon dioxide to form bicarbonate ion and a proton (*1*−*4*). The single divalent zinc ion functions as an electrostatic catalyst that lowers the pK_a of its bound solvent molecule and stabilizes the negative charge of the transition state (*5*). In addition to operating near the limit of diffusion control (*3*), CAII is novel as a metalloprotein due to its unusually high affinity for zinc: the CAII−Zn^{2+} dissociation constant is 1−4 pM (*6*−*7*), and protein-zinc affinity can be engineered by design from micromolar to femtomolar affinity (*5*).

The zinc-binding site of human CAII resides at the bottom of a 15-Å-deep active site cleft as first revealed in the crystal structure of human erythrocyte CAII (*8*−*9*). Analysis of the structure reveals a hierarchy of three conserved features that modulate the properties of the metal binding site (Figure 1). First, three direct ligands from the protein (H94, H96, H119) and a hydroxide ion coordinate to zinc in a tetrahedral array. Second, indirect ligands (or "second-shell" ligands: Q92, E117, and the backbone carbonyl of N244) hydrogen bond to zinc-coordinated histidine residues, and T199 hydrogen bonds to the zinc-bound hydroxide ion. These second-shell interactions enhance the basicity of direct histidine ligands and also help position the direct ligands for optimal metal coordination (*10*−*14*). Third, aromatic residues F93, F95, and W97 anchor the β-strand containing direct ligands H94 and H96 in the hydrophobic core of the enzyme and stabilize its conformation. In catalytically active carbonic anhydrase sequences, Trp is conserved at position 97, while a hydrophobic amino acid (Phe, Leu, Ile, and Met) is retained at

* To whom correspondence should be addressed: Dr. David W. Christianson, e-mail: chris@xtal.chem.upenn.edu, phone: (215) 898-5714, fax: (215) 573-2201.

† Supported by National Institute of Health Grants GM45614 (D.W.C) and GM40602 (C.A.F.).

‡ Atomic coordinates have been deposited in the Research Collaboratory for Structural Bioinformatics (RCSB) with the following accession codes: F95M/W97V, 1FQL; F93I/F95M/W97V, 1FQM; apo-F93I/F95M/W97V, 1FQN; Co^{2+}-F93I/F95M/W97V, 1FQR; Cu^{2+}-F93I/F95M/W97V, 1FR4; F93S/F95L/W97M, 1FR7; apo-F93S/F95L/W97M, 1FSN; Co^{2+}-F93S/F95L/W97M, 1FSQ; Cu^{2+}-F93S/F95L/W97M, 1FSR.

§ University of Pennsylvania.

|| University of Michigan.

[1] Abbreviations: CAII, human carbonic anhydrase II; Tris, tris-(hydroxymethyl)aminoethane; HEPES, 4-(2-hydroxyethyl)piperazine-1-ethanesulfonic acid; PEG, poly(ethylene glycol)

10.1021/bi001649j CCC: $19.00
Published on Web 10/10/2000

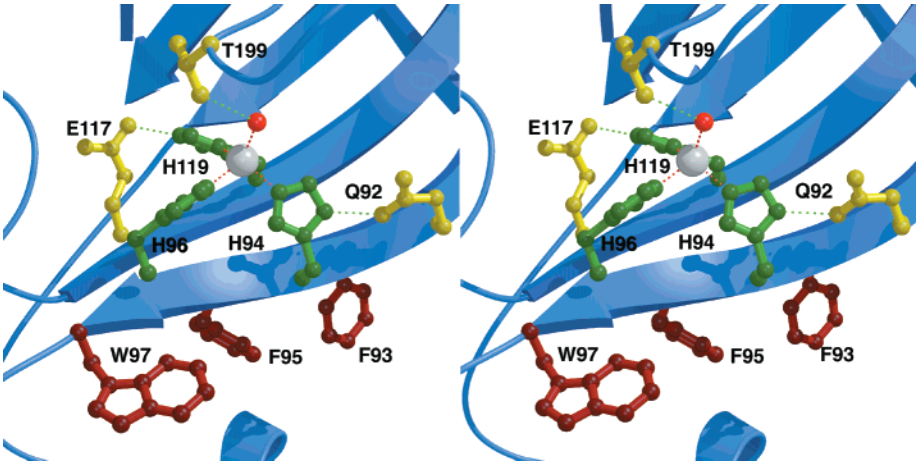

FIGURE 1: Zinc binding site of CAII. Direct metal coordination interactions are indicated by red dashed lines, and indirect (or "second shell") interactions are indicated by green dashed lines. Hydrophobic shell residues W97, F95, and F93 are located on the opposite face of the β-strand containing direct ligands H96 and H94 and indirect ligand Q92. Zinc-bound hydroxide ion appears as a small red sphere.

positions 93 and 95 (*4*). Such "hydrophobic shell" residues are also proposed to enhance protein−metal affinity by establishing a metal site environment with a reduced dielectric constant (*15*): dipole-charge ligand−metal electrostatic interactions should be stronger in a medium of low dielectric.

Wild-type CAII binds a number of other metal ions in the zinc binding site with a coordination geometry characteristic of these metals in protein crystal structures (*9*, *16*). For example, Mn^{2+} and Ni^{2+} bind with octahedral coordination geometry, Co^{2+} binds with tetrahedral coordination geometry, and Cu^{2+} binds with trigonal bipyramidal coordination geometry. Additional molecules from solvent are recruited to increase the coordination number of Mn^{2+}, Ni^{2+}, and Cu^{2+} relative to Zn^{2+} (*9*, *16*). The Mn^{2+} coordination polyhedron is completed by a water molecule and two oxygen atoms from a sulfate anion, while Ni^{2+} is coordinated by two water molecules and a single sulfate oxygen in addition to the histidine protein ligands. Interestingly, Cu^{2+}-bound CAII has one water molecule and an additional molecule interpreted as diatomic oxygen to complete a trigonal bipyramidal coordination polyhedron (*16*). The metal selectivity of wild-type CAII follows the Irving−Williams series (*6*, *17*), although compared to small molecule chelators the specificity of CAII for Zn^{2+} is increased.

The results of recent phage display studies selecting variants with altered zinc affinity are consistent with an important role for hydrophobic shell residues in enhancing metal affinity and equilibration kinetics (*18*). However, it is not clear that these particular residues affect metal binding by modulating the active site dielectric constant. The effective volume of the substituted side chain at positions 93, 95, and 97 strongly correlates with the rate constant of metal dissociation. Intriguingly, substitutions of wild-type aromatic residues at positions 93, 95, and 97 indicate that smaller side chains enhance copper affinity while decreasing enzyme stability, whereas cobalt and zinc affinities are compromised (*19*). These data suggest that the conserved F93/F95/W97 cluster is important for orienting H94 and H96 to stabilize tetrahedral metal coordination geometry while destabilizing trigonal bipyramidal coordination geometry (*19*). Here, we probe the role of the F93/F95/W97 aromatic cluster in modulating metal affinity and specificity by correlating the X-ray crystal structures of three CAII variants, F95M/W97V, F93S/F95L/W97M, and F93I/F95M/W97V CAIIs, with their affinity and specificity for binding Zn^{2+}, Co^{2+}, and Cu^{2+}.

MATERIALS AND METHODS

Crystallography. The F95M/W97V and F93I/F95M/W97V CAII variants were crystallized using the hanging drop vapor diffusion method: 5 μL drops of precipitant buffer containing 50 mM Tris-SO_4 (pH 8.0 at 25 °C) and 2.75−2.85 M $(NH_4)_2SO_4$ were added to 5 μL drops containing approximately 10 mg/mL protein on a silanized cover slip. The cover slip was sealed over a reservoir containing 1 mL of the precipitant buffer. Prior to crystallization, the protein was incubated with 1 mM methyl mercuric acetate to facilitate the formation of large parallelepipedons. Crystals grew in about two weeks at 4 °C and were isomorphous with those of the native erythrocyte and recombinant wild-type enzymes (*8*, *20*); crystals belonged to space group $P2_1$ with unit cell parameters $a = 41.8$ Å, $b = 41.3$ Å, $c = 72.3$ Å, and $\beta = 104.7°$ (one molecule per asymmetric unit). The F93S/F95L/W97M variant was crystallized by precipitation against 100 mM HEPES (pH 7.0 at 25 °C) and 25% PEG 1500; incubation with methyl mercuric acetate was not required for optimal crystal growth. Crystals grew in 2−3 weeks at 4 °C and belonged to space group $P1$ with unit cell dimensions $a = 42.2$ Å, $b = 43.7$ Å, $c = 66.7$ Å, and $\alpha = 86.9°$, $\beta = 89.9°$, $\gamma = 75.9°$ (two molecules per asymmetric unit).

Crystals of the metal-free F93I/F95M/W97V variant were prepared by first dialyzing the mercury out of the crystals by soaking the crystals in 3.0 M $(NH_4)_2SO_4$, 50 mM Tris-SO_4 (pH 8.0 at 25 °C), and 1 mM β-mercaptoethanol for 3 days (mother liquor was changed twice a day). Zinc was dialyzed out by soaking the crystals in 2.8 M $(NH_4)_2SO_4$, 50 mM Tris-SO_4, and 20 mM dipicolinic acid-NaOH (pH 7.0 at 25 °C) for 10−12 days, refreshing the buffer solution once a day. To generate crystals of the metal-free F93S/F95L/W97M variant, zinc was removed from the enzyme active site by dialysis against 100 mM HEPES, 30% PEG 1500, and 20 mM dipicolinic acid-NaOH (pH 7.0 at 25 °C) for 10−12 days (buffer was refreshed once a day). Metal-

Table 1: Data Collection and Refinement Statistics for F93I/F95M/W97V CAII Structures

metal derivative	Zn^{2+}	apo	Co^{2+}	Cu^{2+}
no. of crystals	1	1	1	1
no. of measured reflections	41 762	50 550	45 440	80 681
no. of unique reflections	15 386	16 220	15 578	31 111
resolution range (Å)	20.0−2.0	20.0−2.0	20.0−2.0	20.0−1.6
completeness of data overall (last shell) (%)	93.5 (84.5)	99.3 (94.0)	93.2 (77.7)	96.7 (76.2)
R_{sym} overall (last shell)[a]	0.059 (0.121)	0.068 (0.309)	0.043 (0.156)	0.048 (0.298)
no. of reflections used in refinement (in test set)	14 647 (737)	15 302 (785)	14 800 (770)	29 550 (1542)
R_{cryst} (R_{free})[b]	0.185 (0.268)	0.189 (0.279)	0.216 (0.275)	0.221 (0.259)
no. of water molecules in final cycle of refinement	109	135	80	111
rms deviation from ideal bond lengths (Å)	0.013	0.017	0.007	0.006
rms deviation from ideal bond angles (deg)	1.8	1.9	1.3	1.4
rms deviation from ideal dihedral angles (deg)	25.8	26.2	27.7	27.6
rms deviation from ideal improper dihedral angles (deg)	1.6	1.8	0.6	0.7

[a] R_{sym} for replicate reflections, $R = \Sigma|I_h - \langle I_h\rangle|/\Sigma\langle I_h\rangle$; I_h = intensity measured for reflection h; $\langle I_h\rangle$ = average intensity for reflection h calculated from replicate data. [b] Crystallographic R factor, $R_{cryst} = \Sigma||\boldsymbol{F}_o| - |\boldsymbol{F}_c||/\Sigma|\boldsymbol{F}_o|$ for reflections contained in the working set. Free R factor, $R_{free} = \Sigma||\boldsymbol{F}_o| - |\boldsymbol{F}_c||/\Sigma|\boldsymbol{F}_o|$ for reflections contained in the test set held aside during refinement (5% of total). $|\boldsymbol{F}_o|$ and $|\boldsymbol{F}_c|$ are the observed and calculated structure factor amplitudes, respectively.

substituted F93I/F95M/W97V and F93S/F95L/W97M variants were prepared by soaking apo-enzyme crystals in stabilization buffers of 2.8 M $(NH_4)_2SO_4$, 50 mM Tris-SO_4 (pH 8.0 at 25 °C), and 30% PEG 1500, 100 mM HEPES (pH 7.0 at 25 °C), respectively. Subsequently, crystals were soaked in stabilization buffers containing either 1 mM $CuSO_4$ or $CoCl_2$ for 2 days.

Prior to data collection, crystals were gradually transferred to a cryoprotectant solution containing 20% glycerol in addition to the original precipitant solution and flash-cooled with liquid nitrogen. All intensity data, with the exception of those collected from crystals of Cu^{2+}-F93I/F95M/W97V and Zn^{2+}-F93S/F95L/W97M CAIIs, were collected on an R-AXIS IIc image plate detector. Individual ϕ oscillation images spanning 2° were collected for 15 min each for a total angular sweep of 100 to 180°. A Rigaku RU-200HB rotating anode X-ray generator provided Cu Kα radiation at 50 kV/100 mA (λ = 1.5418 Å). The crystal-to-detector distance was set to 100 mm, and the detector swing angle (2θ) was set to 0°. Intensity data for Cu^{2+}-F93I/F95M/W97V and Zn^{2+}-F93S/F95L/W97M CAIIs were collected at Brookhaven National Laboratory beamline X12B at the National Synchrotron Light Source in Upton, NY. Intensity data integration and reduction was performed using the HKL suite of programs (*21*).

For structure determination of F93I/F95M/W97V CAII by the difference Fourier method, the starting coordinates were those of native CAII less the atoms of the variant side chains and all water molecules. The lone exception was Cu^{2+}-F93I/F95M/W97V CAII, for which initial phasing was achieved by molecular replacement using AMoRe (*22*−*23*); the structure of native CAII less the atoms of variant side chains and all water molecules was used as a search probe. Using intensity data in the 8−3 Å shell with $I > 3\sigma$, the cross rotation search yielded two 36.6σ peaks with $\alpha = 103.20$, $\beta = 114.80$, $\gamma = 265.00°$ and $\alpha = 76.80$, $\beta = 65.20°$, $\gamma = 85.00°$, respectively. Subsequent translation searches yielded peaks at 57.1σ and 58.7σ with fractional coordinates $x = 0.3636$, $y = 0.0000$, $z = 0.1354$ and $x = 0.6416$, $y = 0.5001$, $z = 0.8705$, respectively. The initial R factor was lowered by rigid body refinement from 0.391 to 0.316.

For F93S/F95L/W97M CAII, initial phasing was likewise achieved by molecular replacement with AMoRe (*22*, *23*). Using intensity data in the 8−3 Å shell with $I > 3\sigma$, the cross rotation search yielded 24.7σ and 23.7σ peaks at $\alpha = 230.70°$, $\beta = 139.50°$, $\gamma = 126.30°$ and $\alpha = 44.30°$, $\beta = 145.00°$, $\gamma = 118.70°$, respectively. A translation search with the first molecule fixed yielded a peak at 34.4σ with fractional coordinates $x = 0.7147$, $y = 0.9291$, $z = 0.5019$ for the second molecule. The initial R factor was lowered by rigid body refinement from 0.483 to 0.406. The refined 1.5-Å structure of F93S/F95L/W97M CAII less Zn^{2+} and all water molecules was subsequently used as the starting coordinate set for the structure determinations of metal-free and metal-substituted variant structures.

All structures were refined by simulated annealing ($T_{initial}$ = 3000 K) with energy minimization as implemented in X-PLOR (*24*). After initial rounds of refinement, electron density for each variant side chain was typically clear and unambiguous. The variant side chains, metals, and water molecules were modeled into electron density maps generated with Fourier coefficients $2|F_o| - |F_c|$ and $|F_o| - |F_c|$ and phases calculated from the in-progress atomic model. Iterative rounds of refinement and rebuilding of the models were subsequently achieved with X-PLOR and O (*24*, *25*). Individual B factors were refined, and a bulk solvent correction was applied. Strict noncrystallographic symmetry constraints were used when applicable during refinement, and these were relaxed to appropriately weighted restraints as judged by R_{free}. Refinement ultimately yielded structures with final crystallographic R factors of 0.179−0.244 (R_{free}: 0.250−0.297) and excellent stereochemistry. Data collection and refinement statistics are reported in Tables 1−3. Figures were generated using BOBSCRIPT and Raster3D (*26*, *27*).

RESULTS

F93I/F95M/W97V and F95M/W97V CAIIs. The overall structures of these variant with bound zinc are essentially unchanged relative to wild-type CAII; the rms deviation of 254 Cα atoms are 0.5 and 0.3 Å, respectively. Side chain electron density for the substituted residues is continuous and well-defined; to illustrate, an omit map of F93I/F95M/W97V CAII is presented in Figure 2. Tetrahedral zinc coordination geometry is maintained and the positions of direct ligands H94 and H96 change only slightly, consistent with the high catalytic activities of these variants (*18*). Compensatory plasticity in the hydrophobic core allows for

Table 2: Data Collection and Refinement Statistics for F93S/F95L/W97M CAII Structures

metal derivative	Zn^{2+}	apo	Co^{2+}	Cu^{2+}
no. of crystals	1	1	1	1
no. of measured reflections	221 463	100 913	52 591	30 989
no. of unique reflections	70 629	29 335	29 510	22 676
resolution range (Å)	20.0−1.5	20.0−2.0	20.0−2.0	20.0−2.0
completeness of data overall (last shell) (%)	95.0 (81.2)	93.8 (78.2)	93.5 (78.2)	71.5 (60.1)
R_{sym} overall (last shell)[a]	0.053 (0.374)	0.054 (0.237)	0.057 (0.228)	0.085 (0.371)
no. of reflections used in refinement (in test set)	67 032 (3597)	26 778 (1375)	26 431 (1455)	21 075 (1105)
R_{cryst} (R_{free})[b]	0.240 (0.260)	0.244 (0.291)	0.217 (0.250)	0.240 (0.297)
no. of water molecules in final cycle of refinement	249	135	101	152
rms deviation from ideal bond lengths (Å)	0.005	0.007	0.006	0.008
rms deviation from ideal bond angles (°)	1.3	1.3	1.3	1.5
rms deviation from ideal dihedral angles (°)	27.2	27.7	28.3	28.4
rms deviation from ideal improper dihedral angles (°)	0.7	0.7	0.7	0.7

[a] R_{sym} for replicate reflections, $R = \Sigma|I_h - \langle I_h\rangle|/\Sigma\langle I_h\rangle$; I_h = intensity measured for reflection h; $\langle I_h\rangle$ = average intensity for reflection h calculated from replicate data. [b] Crystallographic R factor, $R_{cryst} = \Sigma||\boldsymbol{F}_o| - |\boldsymbol{F}_c||/\Sigma|\boldsymbol{F}_o|$ for reflections contained in the working set. Free R factor, $R_{free} = \Sigma||\boldsymbol{F}_o| - |\boldsymbol{F}_c||/\Sigma|\boldsymbol{F}_o|$ for reflections contained in the test set held aside during refinement (5% of total). $|\boldsymbol{F}_o|$ and $|\boldsymbol{F}_c|$ are the observed and calculated structure factor amplitudes, respectively

Table 3: Data Collection and Refinement Statistics for F95M/W97V CAII

no. of crystals	2
no. of measured reflections	47 685
no. of unique reflections	15 913
resolution range (Å)	20.0−2.0
completeness of data overall (last shell) (%)	94.9 (88.3)
R_{sym} overall (last shell)[a]	0.079 (0.149)
no. of reflections used in refinement (in test set)	15 140 (764)
R_{cryst} (R_{free})[b]	0.179 (0.255)
no. of water molecules in final cycle of refinement	60
rms deviation from ideal bond lengths (Å)	0.013
rms deviation from ideal bond angles (deg)	1.8
rms deviation from ideal dihedral angles (deg)	26.0
rms deviation from ideal improper dihedral angles (deg)	1.5

[a] R_{sym} for replicate reflections, $R = \Sigma|I_h - \langle I_h\rangle|/\Sigma\langle I_h\rangle$; I_h = intensity measured for reflection h; $\langle I_h\rangle$ = average intensity for reflection **h** calculated from replicate data. [b] Crystallographic R factor, $R_{cryst} = \Sigma||\boldsymbol{F}_o| - |\boldsymbol{F}_c||/\Sigma|\boldsymbol{F}_o|$ for reflections contained in the working set. Free R factor, $R_{free} = \Sigma||\boldsymbol{F}_o| - |\boldsymbol{F}_c||/\Sigma|\boldsymbol{F}_o|$ for reflections contained in the test set held aside during refinement (5% of total). $|\boldsymbol{F}_o|$ and $|\boldsymbol{F}_c|$ are the observed and calculated structure factor amplitudes, respectively.

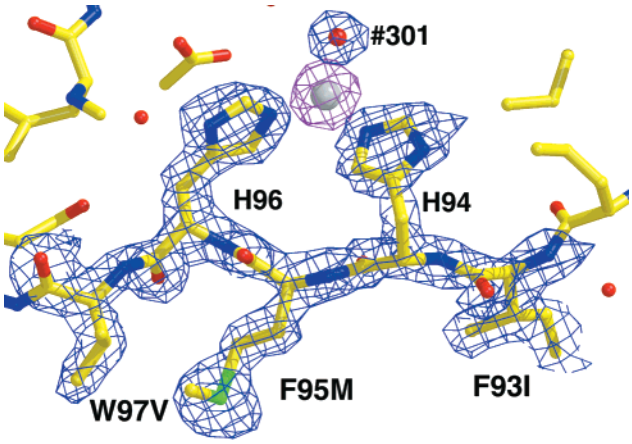

FIGURE 2: Omit maps of the β-strand containing the F93I/F95M/W97V substitutions contoured at 2.7σ (blue map; I93−V97 and zinc-bound hydroxide omitted from structure factor calculation) and 4.5σ (magenta map; Zn^{2+} omitted from structure factor calculation). Refined atomic coordinates are superimposed and color-coded by atom type (C = yellow, N = blue, O = red, S = green; Zn^{2+} appears as a white sphere). Zinc-bound hydroxide ion and other solvent molecules appear as small red spheres.

structural reorganization triggered by substitution of smaller amino acid side chains (Figure 3). For example, in F93I/F95M/W97V CAII, F179 moves toward the void created by the F93I substitution, and F226 and L157 move toward the void created by the F95M substitution. Except for the movement of F179, similar compensatory structural changes are observed in the F95M/W97V double variant (data not shown).

Despite the compensatory structural changes that accompany the large → small amino acid substitutions, significant cavities are introduced in the hydrophobic core adjacent to the substituted amino acids. In F93I/F95M/W97V CAII, two buried water molecules (#310 and #321) partially fill the void created by the F95M and W97V substitutions; water #310 hydrogen bonds with water #321, which in turn hydrogen bonds with the backbone NH group of F66 and the carbonyl oxygen of M95. Another cavity is adjacent to the D71−K76 loop and is relatively distant from the sites of substitution (~13 Å). A water molecule (#304) fills this void and hydrogen bonds to the backbone carbonyl oxygen of Q74 and the backbone NH group of K76. This cavity is also observed in the wild-type enzyme and is occupied by three water molecules.

The difference electron density map of metal-free F93I/F95M/W97V CAII reveals no density corresponding to an active site zinc ion (data not shown). Instead, a water molecule (#301) hydrogen bonds to zinc ligands H96 and H119; this water is located 1.3 Å away from the former position of the zinc ion. Surprisingly, the third ligand, H94, rotates approximately 90° away from the former zinc site (Figure 4). The side chain of Q92, which hydrogen bonds to H94 in the zinc-bound structure, also rotates away from the active site and remains hydrogen bonded to H94 in the metal-free structure. In marked contrast, zinc dissociation from wild-type CAII does not trigger such conformational changes (*9*). Interestingly, conformational changes accompanying zinc loss increase the volume of cavity defects by ~70 $Å^3$, which presumably contributes to destabilization of the metal-free state.

The Co^{2+}-F93I/F95M/W97V CAII structure is very similar to the Zn^{2+}-F93I/F95M/W97V CAII structure; the rms deviation of 254 Cα atoms between the two structures is 0.2 Å. The Co^{2+} ion binds in the same location as zinc and

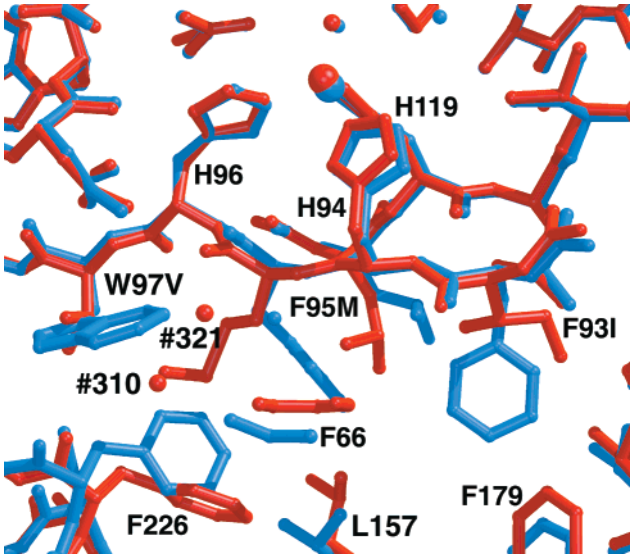

FIGURE 3: Superposition of wild-type (blue) and F93I/F95M/W97V (red) CAIIs. Zinc ions appear as large spheres, and solvent molecules appear as small spheres. Note that the zinc coordination environment remains relatively unchanged; however, significant compensatory structural changes occur in the hydrophobic core to accommodate the triple amino acid substitution. Solvent molecules #310 and #321 partially fill the void created by the F95M and W97V substitutions.

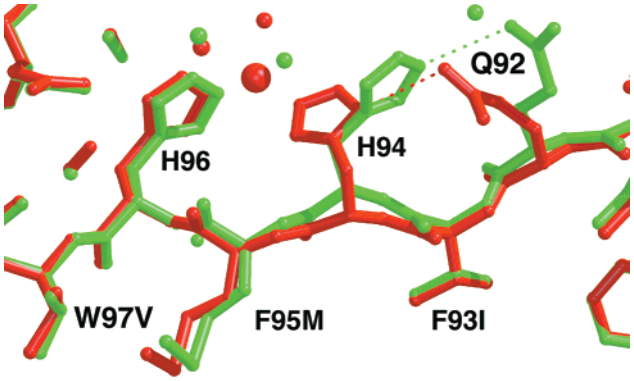

FIGURE 4: Superposition of zinc-bound (red) and zinc-free (green) F93I/F95M/W97V CAII structures. Note the significant conformational changes of direct ligand H94 and its indirect ligand partner Q92. The H94−Q92 hydrogen bond interaction is maintained despite this conformational change. This conformational change does not accompany zinc dissociation from the wild-type enzyme (Håkansson et al., 1992). The zinc ion appears as a large sphere and solvent molecules appear as small spheres. Hydrogen bonds are indicated by dashed lines.

maintains an identical tetrahedral coordination environment; no significant changes are observed in the metal binding site or the hydrophobic shell residues, and no changes are observed in the volumes of introduced cavities (data not shown). In contrast, the Cu^{2+}-F93I/F95M/W97V CAII structure reveals a change in geometry to 5-coordinate square pyramidal due to the addition of sulfate anion to the metal coordination polyhedron (Figure 5). The side chain of H94 occupies the apical coordination site and H119, H96, a sulfate oxygen, and a solvent molecule occupy equatorial coordination sites. Otherwise, the conformations of active site residues Cu^{2+}-F93I/F95M/W97V CAII are very similar to those found in Zn^{2+}-F93I/F95M/W97V CAII. Cavities in Cu^{2+}-F93I/F95M/W97V CAII are very similar to those found in Zn^{2+}-F93I/F95M/W97V CAII. The active site structure of Co^{2+}-F93I/F95M/W97V CAII is overall very similar to that of Co^{2+}-bound wild-type CAII. The lone exception in Co^{2+}-bound wild-type CAII is the displacement of the deep water with a molecule interpreted as diatomic oxygen. This molecule does not coordinate to cobalt (*16*). F93I/F95M/W97V and wild-type CAIIs both bind Cu^{2+} with 5-coordinate geometry, but small differences in the metal ligands cause the coordination geometry to resemble trigonal bipyramidal in wild-type CAII and square pyramidal in Cu^{2+}-F93I/F95M/W97V CAII. The fifth ligand in Cu^{2+}-bound wild-type CAII is modeled as molecular oxygen, whereas this ligand is an oxygen from a sulfate anion in Cu^{2+}-F93I/F95M/W97V CAII.

F93S/F95L/W97M CAII. The overall structure of this variant is essentially unchanged relative to the wild-type enzyme, with which the rms deviation of 254 Cα atoms is 0.6 Å. Side chain electron density for the substituted residues is continuous and well-defined (data not shown). Tetrahedral zinc coordination is maintained in this variant despite the substitution of smaller side chains for the aromatic residues in the hydrophobic core and despite the segmental movement of the β-strand flanking zinc ligand H94. In this mutant, the position of the zinc-bound water molecule is altered slightly, perhaps explaining the reduction in CO_2 hydrase activity (*18*). As seen in F93I/F95M/W97V CAII, the plasticity of the hydrophobic core enables neighboring residues to undergo compensatory movements to minimize the introduced volume defects. For example, F179, V160, F66, and F226 all make significant movements to partially fill the void left by the variant side chains (Figure 6). As observed in F93I/F95M/W97V CAII, two water molecules (#421 and #369) help to fill the void created by the F95L and W97M substitutions; water #421 hydrogen bonds with the carbonyl oxygen of M241, the carbonyl oxygen of F226, and another water molecule (#369), which in turn hydrogen bonds with carbonyl oxygen of L95 and the backbone nitrogen of F66.

The difference electron density map of metal-free F93S/F95L/W97M CAII reveals no density corresponding to an active site zinc ion (data not shown). Instead a water molecule (#302) is located 1.1 Å away from the former position of the zinc ion and hydrogen bonds to H96, H119, and a second water molecule (#372). As observed in metal-free F93I/F95M/F97V CAII, H94 and Q92 are rotated away from the active site yet maintain their hydrogen bond interaction (data not shown). As mentioned previously, zinc dissociation from wild-type CAII does not trigger the H94-Q92 conformational change (*9*).

The structure of Co^{2+}-F93S/F95L/W97M CAII reveals a change in metal ion coordination geometry to 5-coordinate trigonal bipyramidal due to the addition of a solvent molecule and an unidentified molecule that we interpret as azide anion (data not shown). The side chain of H96 and an azide nitrogen serve as axial ligands and H119, H94, and a solvent molecule serve as equatorial ligands. The rms deviation of 254 Cα atoms between the two structures is 0.2 Å. It is notable that F93S/F95L/W97M CAII exhibits greater flexibility than F93I/F95M/F97V CAII, in that it binds Co^{2+} with nontetrahedral coordination geometry. In the absence of azide, the absorbance spectrum characteristic of a tetrahedral cobalt ion and the high catalytic activity suggest that F93S/F95L/W97M CAII binds cobalt in tetrahedral geometry (*19*),

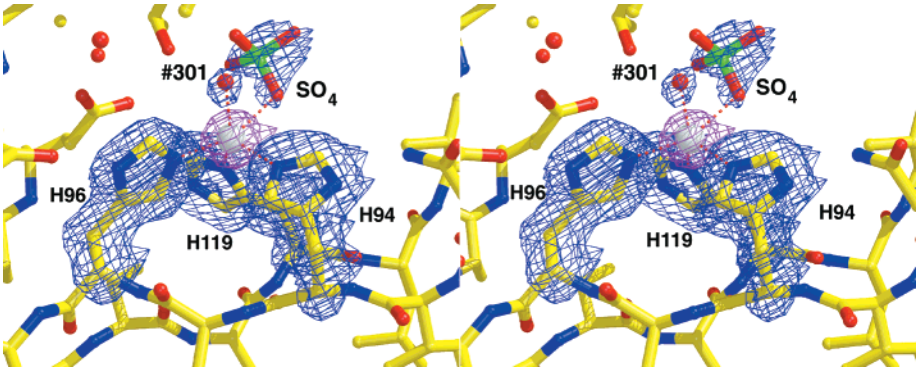

FIGURE 5: Omit maps of Cu^{2+}-F93I/F95M/W97V CAII contoured at 3.0σ (blue map; side chain atoms of H94, H96, H119, and copper-bound hydroxide and sulfate ions omitted from structure factor calculation) and 5.0σ (magenta map; Cu^{2+} omitted from structure factor calculation). Refined atomic coordinates are superimposed and color-coded by atom type (C = yellow, N = blue, O = red, S = green; Cu^{2+} appears as a white sphere). Note that the metal coordination number increases to 5 with square pyramidal geometry due to the binding of the sulfate anion.

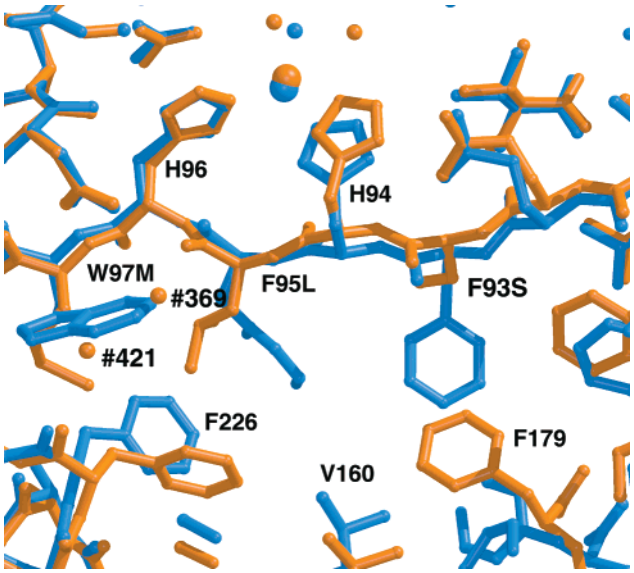

FIGURE 6: Superposition of wild-type (blue) and F93S/F95L/W97M (orange) CAIIs. Zinc ions appear as large spheres and solvent molecules appear as small spheres. Note that the zinc coordination environment remains relatively unchanged; however, small structural changes in the β-strand and significant compensatory movements of amino acid side chains occur in the hydrophobic core to accommodate the triple amino acid substitution. Solvent molecules #421 and #369 partially fill the void created by the F95L and W97M substitutions.

further indicating the flexibility of the metal site in this variant.

The structure of Cu^{2+}-F93S/F95L/W97M CAII also exhibits a change in metal ion coordination geometry to 5-coordinate trigonal bipyramidal. Again, mutation of the anchoring hydrophobic residues increases the flexibility of the CAII variant allowing nontetrahedral metal coordination polyhedra to form more readily than in the wild-type enzyme. In this structure, the molecular basis for enhanced Cu^{2+} affinity (K_d = 2 fM) (*19*) is revealed; an electron density map is found in Figure 7. The side chain of H96 and a solvent molecule (#302) occupy apical coordination sites and H119, H94, and a solvent molecule (#301) occupy equatorial coordination sites. Active site residues in Cu^{2+}-F93S/F95L/W97M CAII shift slightly relative to those found in Zn^{2+}-F93S/F95L/W97M CAII to accommodate the change in coordination geometry. Co^{2+}-F93S/F95L/W97M CAII also differs from Co^{2+}-bound wild-type CAII, which has tetrahedral metal coordination geometry. Interestingly, Co^{2+}-bound wild-type CAII also has an unidentified molecule near the active site, but unlike the azide anion modeled in Co^{2+}-F93S/F95L/W97M CAII, this molecule does not coordinate to Co^{2+} in the wild-type enzyme. The Cu^{2+} ion binds both F93S/F95L/W97M and wild-type CAIIs with roughly trigonal bipyramidal coordination geometry (Table 4). However, Cu^{2+}-F93S/F95L/W97M CAII recruits two water molecules to complete its metal coordination polyhedron, whereas Cu^{2+} is bound by a water molecule and an oxygen from diatomic oxygen in wild-type.

DISCUSSION

Although the overall structural differences between each CAII variant described and the wild-type enzyme are relatively small, it is clear that the wild-type aromatic residues F93, F95, and W97 serve as anchors that help to preorient and stabilize the direct metal ligands in a tetrahedral array to optimize zinc binding. In accord with these structural results, we recently demonstrated that these hydrophobic residues are important for maintaining high zinc affinity and slow zinc dissociation rate constants (*18*) as well as determining metal binding specificity and enhancing CAII stability (*19*). Substitutions of these aromatic residues with smaller side chains increase copper affinity while decreasing the affinity of cobalt and zinc. The structures reported herein illuminate the molecular basis of affinity variations, and the geometries and affinities of metal coordination polyhedra are summarized in Table 4. In wild-type CAII, the geometries of the metal coordination polyhedra reflect the preference of the metal studied: tetrahedral geometry for zinc and cobalt, and trigonal bipyramidal geometry for copper (*9*, *16*). Mutations of the hydrophobic residues that anchor and preorient the direct metal ligands H94 and H96 for tetrahedral coordination geometry weaken the anchor, as indicated by the H94−Q92 conformational change in the metal-free variants (Figure 4). This enhances the formation of nontetrahedral coordination geometries upon the binding of metal ions, which appears to be a most favorable consequence for Cu^{2+} binding at the expense of Zn^{2+} binding.

Despite the flexibility introduced in the metal coordination polyhedron by amino acid substitutions at positions 93, 95,

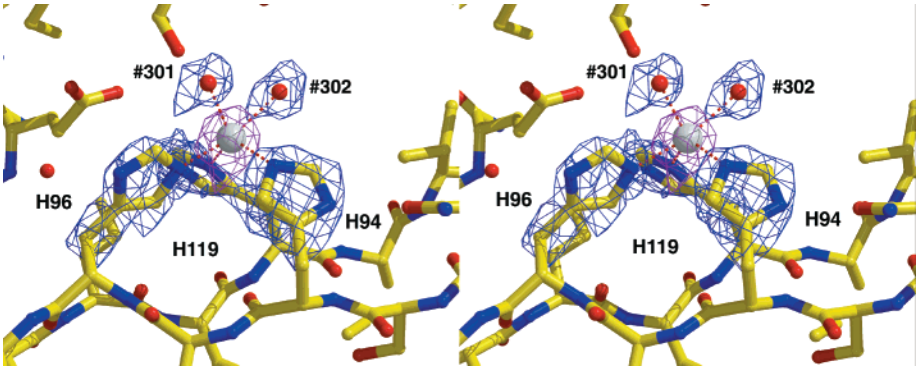

FIGURE 7: Omit maps of Cu^{2+}-F93S/F95L/W97M CAII contoured at 7.0σ (blue map; side chain atoms of H94, H96, H119, and two zinc-bound hydroxide ions omitted from structure factor calculation) and 10.0σ (magenta map; Cu^{2+} omitted from structure factor calculation). Refined atomic coordinates are superimposed and color-coded by atom type (C = yellow, N = blue, O = red, S = green; Cu^{2+} appears as a white sphere). Note that the metal coordination number increases to 5 with trigonal bipyramidal geometry upon the binding of Cu^{2+} to this variant.

Table 4: Deviations from Ideal Tetrahedral Metal Coordination Geometry

		Zn^{2+}		Co^{2+}		Cu^{2+}	
		angle (deg)	Δ^a	angle (deg)	Δ^a	angle (deg)	Δ^a
wild-type CAII	H94−M^{2+}−H96	103.9	5.6	105.3	4.2	92.9	16.6
	H94−M^{2+}−H119	115.3	5.8	116.2	6.7	118.3	8.8
	H96− M^{2+}−H119	99.2	10.3	99.3	10.2	95.6	13.9
	total deviation		21.7		21.1		39.3
	overall geometry	tetrahedral		tetrahedral		trigonal bipyramidal	
	K_d	0.8 pM[b]		20 ± 14 nM[c]		17 ± 4 fM[c]	
F93I/F95M/W97V CAII	H94−M^{2+}−H96	100.9	8.6	107.3	2.2	105.6	3.9
	H94−M^{2+}−H119	107.9	1.6	103.9	5.6	112.6	3.1
	H96−M^{2+}−H119	102.4	7.1	104.0	5.5	95.8	13.7
	total deviation		17.3		13.3		20.7
	overall geometry	tetrahedral		tetrahedral		square pyramidal[d]	
	K_d	11 pM[b]		66 ± 24 nM[c]		3 ± 1 fM[c]	
F93S/F95L/W97M CAII	H94−M^{2+}−H96	121.3	11.8	107.2	2.3	94.9	14.6
	H94−M^{2+}−H119	107.4	2.1	117.2	7.7	122.5	13
	H96−M^{2+}−H119	102.6	6.9	88.2	21.3	81.5	28
	total deviation		20.8		31.3		55.6
	overall geometry	tetrahedral		trigonal bipyramidal		trigonal bipyramidal	
	K_d	29 pM[b]		145 ± 100 nM[c]		2 ± 1 fM[c]	

[a] Individual angular deviation from ideal tetrahedral geometry, 109.5°. [b] Ref *18*. [c] Ref *19*. [d] Despite the relative small deviation from ideal tetrahedral geometry for the histidine ligands, the incorporation of a fifth ligand in binding Cu^{2+} suggests that square pyramidal with coordination number = 5 is the more correct assignment of overall geometry.

and 97, all Zn^{2+}-bound CAII variants adopt tetrahedral metal coordination geometry similar to that observed in the wild-type enzyme. Deviations from ideal tetrahedral metal coordination geometry for the three protein ligands H94, H96, and H119 are greatest for Cu^{2+}-bound CAII variants, reflecting the change to an alternative coordination geometry (Table 4). We conclude that the substitution of smaller hydrophobic side chains for bulky, aromatic core residues decreases the free energy barrier for adopting nontetrahedral metal coordination geometries. The ~0.7-Å segmental movement of the β-strand containing metal ligands H94 and H96 in F93S/F95L/W97M CAII (Figure 6) illustrates the compensatory flexibility that may similarly contribute to altered metal specificity. Of the variants investigated, F93S/F95L/W97M CAII exhibits both the largest enhancement of Cu^{2+} affinity [8.5-fold tighter than wild-type CAII (Table 4)] and the largest decrease in Zn^{2+} affinity (36-fold). These changes in metal affinity lead to an enhancement in the copper specificity as indicated by the ratio of the metal dissociation constants for F93S/F95L/W97M CAII (the comparable wild-type CAII ratios are shown in parentheses): $K_{Zn}/K_{Cu} = 1.4 \times 10^4$ (4.7×10^1) and $K_{Co}/K_{Cu} = 7 \times 10^7$ (1×10^6). The altered geometry of Co^{2+} -F93S/F95L/W97M CAII is consistent with the increased flexibility of the metal site in this variant.

Interestingly, hydrophobic side chain substitutions introduce cavities in the hydrophobic core of the enzyme, but the volumes of these cavities do not generally correlate with metal affinity in the entire series of metal-bound CAII variants. However, these cavities must certainly contribute to the decreased stability (up to 4 kcal/mol) of both the metal-free and metal-bound forms of the hydrophobic core mutants, as indicated by guanidine hydrochloride-induced denaturation experiments (*19*). The stabilities of the variant CAIIs directly correlate with the hydrophobicities of the substituted amino acids (*19*). X-ray crystal structures of F95M/W97V, F93I/F95M/W97V, and F93S/F95L/W97M CAIIs reveal the introduction of new cavities in the hydrophobic core, compensatory movements of surrounding side chains, and the incorporation of buried water molecules. Structure−stability relationships for internal cavities in proteins have been analyzed in detail (*28*−*30*). According to these studies, buried cavities are likely to be hydrated (*28*), and cavities larger than 50 Å^3 are rarely empty (*29*). The probability of hydration

increases with increasing size of the cavity and the number of hydrogen bond donor/acceptors, with each additional bond stabilizing the folded conformation by 0.6 kcal/mol (*28*). A buried solvent molecule will usually have three hydrogen bond donor/acceptors (*28*−*30*).

The cavities introduced into CAII variants are consistent with these structure−stability relationships. The zinc-bound CAII variants contain cavities ranging in size from 7 to 78 Å^3. Three main cavities unique to the variants are located adjacent to each point of mutation (F93, F95, and W97) in the hydrophobic core of the enzyme. Predictably, no cavity is observed near F93 in F95M/W97V CAII, and two additional cavities are observed adjacent to S93 in F93S/F95L/W97M CAII. Cavities larger than 50 Å^3 are indeed solvated with one exception: an empty 73 Å^3 cavity adjacent to S93 in F93S/F95L/W97M CAII which is larger than its counterpart in F93I/F95M/W97V CAII (34 Å^3). The 73 Å^3 empty cavity in F93S/F95L/W97M CAII may contribute to its decreased stability (1.3−1.7 kcal/mol) relative to the F93I/F95M/W97V CAII variant (Hunt et al., 1999). Buried solvent molecules have either 2 or 3 hydrogen bond donor/acceptors in the CAII variant structures.

The Cu^{2+} affinities of CAII variants correlate well with the hydrophobicity and size of amino acids substituted at positions F93, F95, and W97 (*19*). However, unlike the trends observed for Zn^{2+} and Co^{2+} binding, where affinity decreases upon the substitution of smaller residues in the core, Cu^{2+} affinity is enhanced by substitutions that apparently "loosen" the histidine ligands that are rigidly preoriented in a tetrahedral array in the wild-type enzyme. Whereas wild-type CAII binds Cu^{2+} with trigonal bipyramidal geometry (*16*), formation of this nontetrahedral site is energetically unfavorable (*19*). Therefore, increased flexibility enhances formation of 5-coordinate trigonal bipyramidal or square pyramidal metal coordination geometry relative to 4-coordinate tetrahedral geometry, which in turn increases Cu^{2+} affinity.

In closing, the key finding of this work is that aromatic core residues in wild-type CAII serve as anchors that help to preorient direct metal ligands and second-shell metal ligands to optimize zinc binding geometry and destabilize alternative geometries. Although the contribution of these hydrophobic residues to a favorable dielectric contrast for metal binding is possible (*15*), this effect is likely swamped by the role of F93, F95, and W97 in anchoring the conformation of the β-strand containing direct zinc ligands H94 and H96 and second-shell ligand Q92. These structural insights on the influence of hydrophobic core residues on metal binding and specificity suggest a general rationale for their persistence in evolution: geometrical constraints imposed by the preorientation of direct and second-shell metal ligands to form tetrahedral metal coordination geometry, and the relative destabilization of alternative metal geometries, are likely to be the main determinants of enhanced Zn^{2+}/Cu^{2+} binding and specificity.

ACKNOWLEDGMENT

We thank Abe Pachikara for assistance with crystal growth.

REFERENCES

1. Coleman, J. E. (1967) *J. Biol. Chem. 242*, 5212−5219.
2. Lindskog, S., and Coleman, J. E. (1973) *Proc. Natl. Acad. Sci. U.S.A. 70*, 2505−2508.
3. Silverman, D. N., and Lindskog, S. (1988) *Acc. Chem. Res. 21*, 30−36.
4. Hewett-Emmett, D., and Tashian, R. E. (1996) *Mol. Phylogenet. Evol. 5*, 50−77.
5. Christianson, D. W., and Fierke, C. A. (1996) *Acc. Chem. Res. 29*, 331−339.
6. Lindskog, S., and Nyman, P. O. (1964) *Biochim. Biophys. Acta 85*, 462−474.
7. Kiefer, L. L., Krebs, J. F., Paterno, S. A., and Fierke, C. A. (1993) *Biochemistry 32*, 9896−9900.
8. Liljas, A., Kannan, K. K., Bergstén, P.-C., Waara, I., Fridborg, K., Strandberg, B., Carlbom, U., Järup, L., Lövgren, S., and Petef, M. (1972) *Nature (London), New Biol. 235*, 131−137.
9. Håkansson, K., Carlsson, M., Svensson, L. A., and Liljas, A. (1992) *J. Mol. Biol. 227*, 1192−1204.
10. Christianson, D. W., and Alexander, R. S. (1989) *J. Am. Chem. Soc. 111*, 6412−6419.
11. Christianson, D. W. (1991) *Adv. Protein Chem. 42*, 281−355.
12. Kiefer, L. L., Paterno, S. A., and Fierke, C. A. (1995) *J. Am. Chem. Soc. 117*, 6831−6837.
13. Lesburg, C. A., and Christianson, D. W. (1995) *J. Am. Chem. Soc. 117*, 6838−6844.
14. Huang, C.-c., Lesburg, C. A., Kiefer, L. L., Fierke, C. A., and Christianson, D. W. (1996) *Biochemistry 35*, 3439−3446.
15. Yamashita, M. M., Wesson, L., Eisenman, G., and Eisenberg, D. (1990) *Proc. Natl. Acad. Sci. U.S.A. 87*, 5648−5652.
16. Håkansson, K., Wehnert, A., and Liljas, A. (1994) *Acta Crystallogr. D50*, 93−100.
17. McCall, K. A., and Fierke, C. A. (2000). *Anal. Biochem. 284*, 307−315.
18. Hunt, J. A., and Fierke, C. A. (1997) *J. Biol. Chem. 272*, 20364−20372.
19. Hunt, J. A., Ahmed, M., and Fierke, C. A. (1999) *Biochemistry 38*, 9054−9062.
20. Alexander, R. S., Nair, S. K., and Christianson, D. W. (1991) *Biochemistry 30*,11064−11072.
21. Otwinowski, Z., and Minor, W. (1997) *Methods Enzymol. 276*, 307−326.
22. Navaza, J. (1994) *Acta Crystallogr. A50*, 157−163.
23. Collaborative Computational Project, No. 4. (1994) *Acta Crystallogr. D50*, 760−763.
24. Brünger, A. T., Kuriyan, J., and Karplus, M. (1987) *Science 235*, 458−460
25. Jones, T. A., Zou, J.-Y., Cowan, S. W., and Kjeldgaard, M. (1991) *Acta Crystallogr. A47*, 110−119.
26. Esnouf, R. M. (1997) *J. Mol. Graphics 15*, 132−134.
27. Merritt, E. A., and Bacon, D. J. (1997) *Methods Enzymol. 277*, 505−524.
28. Williams, M. A., Goodfellow, J. M., and Thornton, J. M. (1994) *Protein Sci. 3*, 1224−1235.
29. Hubbard, S. J., Gross, K.-H, and Argos, P. (1994) *Protein Eng. 7*, 613−626.
30. Hubbard, S. J., and Argos, P. (1995) *Protein Eng. 8*, 1011−1015.

BI001649J